THE ROYAL SOCIETY

A numerical study of submarine-landslide-generated waves and run-up

By Patrick Lynett and Philip L.-F. Liu

School of Civil and Environmental Engineering,
Cornell University, Ithaca, NY 14853, USA

A mathematical model is derived to describe the generation and propagation of water waves by a submarine landslide. The model consists of a depth-integrated continuity equation and momentum equations, in which the ground movement is the forcing function. These equations include full nonlinear, but weak frequency-dispersion, effects. The model is capable of describing wave propagation from relatively deep water to shallow water. Simplified models for waves generated by small seafloor displacement or creeping ground movement are also presented. A numerical algorithm is developed for the general fully nonlinear model. Comparisons are made with a boundary integral equation method model, and a deep-water limit for the depth-integrated model is determined in terms of a characteristic side length of the submarine mass. The importance of nonlinearity and frequency dispersion in the wave-generation region and on the shoreline movement is discussed.

Keywords: landslide tsunamis; Boussinesq equations; wave run-up

1. Introduction

In recent years, significant advances have been made in developing mathematical models to describe the entire process of generation, propagation and run-up of a tsunami event (e.g. Yeh *et al.* 1996; Geist 1998). These models are based primarily on the shallow-water wave equations and are adequate for tsunamis generated by seismic seafloor deformation. Since the duration of the seismic seafloor deformation is very short, the water-surface response is almost instantaneous and the initial water-surface profile mimics the final seafloor deformation. The typical wavelength of this type of tsunami ranges from 20 to 100 km. Therefore, frequency dispersion can be ignored in the generation region. The nonlinearity is also usually not important in the generation region, because the initial wave amplitude is relatively small compared to the wavelength and the water depth. However, the frequency dispersion becomes important when a tsunami propagates for a long distance. Nonlinearity could also dominate as a tsunami enters the run-up phase. Consequently, a complete model that can describe the entire process of tsunami generation, evolution and run-up needs to consider both frequency dispersion and nonlinearity.

Tsunamis are also generated by other mechanisms. For example, submarine landslides have been documented as one of many possible sources for several destructive

Proc. R. Soc. Lond. A (2002) **458**, 2885–2910

2885

tsunamis (Moore & Moore 1984; von Huene *et al*. 1989; Jiang & LeBlond 1992; Tappin *et al*. 1999; Keating & McGuire 2002). On 29 November 1975, a landslide was triggered by a 7.2-magnitude earthquake along the southeast coast of Hawaii. A 60 km stretch of Kilauea's south coast subsided 3.5 m and moved seaward 8 m. This landslide generated a local tsunami with a maximum run-up height of 16 m at Keauhou (Cox & Morgan 1977). More recently, the devastating Papua New Guinea tsunami in 1998 is thought to have been caused by a submarine landslide (Tappin *et al*. 1999, 2001; Keating & McGuire 2002). In terms of tsunami-generation mechanisms, two significant differences exist between submarine-landslide and coseismic seafloor deformation. First, the duration of a landslide is much longer and is in the order of magnitude of several minutes. Hence the time-history of the seafloor movement will affect the characteristics of the generated wave and needs to be included in the model. Secondly, the effective size of the landslide region is usually much smaller than the coseismic seafloor-deformation zone. Consequently, the typical wavelength of the tsunamis generated by a submarine landslide is also shorter, i.e. *ca*. 1–10 km. Therefore, the frequency dispersion could be important in the wave-generation region. The existing numerical models based on shallow-water wave equations may not be suitable for modelling the entire process of submarine-landslide-generated tsunami (e.g. Raney & Butler 1976; Harbitz *et al*. 1993).

In this paper, we shall present a new model describing the generation and propagation of tsunamis by a submarine landslide. In this general model, only the assumption of weak frequency dispersion is employed, i.e. the ratio of water depth to wavelength is small or $O(\mu^2) \ll 1$. Until the past decade, weakly dispersive models were formulated in terms of a depth-averaged velocity (e.g. Peregrine 1967). Recent work has clearly demonstrated that modifications to the frequency dispersion terms (Madsen & Sorensen 1992) or expression of the model equations in terms of an arbitrary-level velocity (Nwogu 1993; Liu 1994) can extend the validity of the linear-dispersion properties into deeper water. The general guideline for dispersive properties is that the 'extended' versions of the depth-integrated equations are valid for wavelengths greater than two water depths, whereas the depth-averaged model is valid for lengths greater than five water depths (e.g. Nwogu 1993). Moreover, in the model presented in this paper, the full nonlinear effect is included, i.e. the ratio of wave amplitude to water depth is of order one or $\varepsilon = O(1)$. Therefore, this new model is more general than that developed by Liu & Earickson (1983), in which the Boussinesq approximation, i.e. $O(\mu^2) = O(\varepsilon) \ll 1$, was used. In the special case where the seafloor is stationary, the new model reduces to the model for fully nonlinear and weakly dispersive waves propagating over a varying water depth (e.g. Liu 1994; Madsen & Schäffer 1998). The model is applicable for both the impulsive slide movement and creeping slide movement. In the latter case, the time duration for the slide is much longer than the characteristic wave period.

This paper is organized as follows. Governing equations and boundary conditions for flow motions generated by a ground movement are summarized in the next section. The derivation of approximate two-dimensional depth-integrated governing equations follows. The general model equations are then simplified for special cases. A numerical algorithm is presented to solve the general mathematical model. The numerical model is tested using available experimental data (e.g. Hammack 1973) for one-dimensional situations. Employing a boundary integral equation model (BIEM), which solves for potential flow in the vertical plane, a deep-water limit for waves generated by
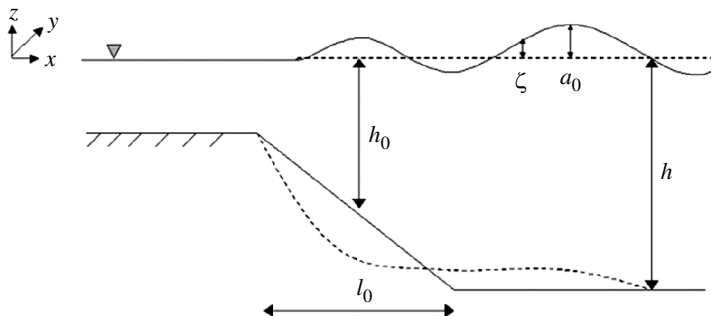
Figure 1. Basic formulational set-up.

submarine slides is determined for the depth-integrated model. The importance of nonlinearity and frequency dispersion is inferred through numerical simulation of a large number of different physical set-ups.

2. Governing equations and boundary conditions

As shown in figure 1, $\zeta'(x', y', t')$ denotes the free-surface displacement of a wave train propagating in the water depth $h'(x', y', t')$. Introducing the characteristic water depth h_0 as the vertical length-scale, the characteristic length of the submarine slide region ℓ_0 as the horizontal length-scale, $\ell_0/\sqrt{gh_0}$ as the time-scale, and the characteristic wave amplitude a_0 as the scale of wave motion, we can define the following dimensionless variables,

$$(x, y) = \frac{(x', y')}{\ell_0}, \qquad z = \frac{z'}{h_0}, \qquad t = \frac{\sqrt{gh_0}t'}{\ell_0},$$

$$h = \frac{h'}{h_0}, \qquad \zeta = \frac{\zeta'}{a_0}, \qquad p = \frac{p'}{\rho g a_0}$$

and

$$(u, v) = \frac{(u', v')}{\varepsilon\sqrt{gh_0}}, \qquad w = \frac{w'}{(\varepsilon/\mu)\sqrt{gh_0}}, \tag{2.1}$$

in which (u, v) represents the horizontal velocity components, w the vertical velocity component, and p the pressure. Two dimensionless parameters have been introduced in (2.1), which are

$$\varepsilon = \frac{a_0}{h_0}, \qquad \mu = \frac{h_0}{\ell_0}. \tag{2.2}$$

Assuming that the viscous effects are insignificant, the wave motion can be described by the continuity equation and Euler's equations, i.e.

$$\mu^2 \nabla \cdot \boldsymbol{u} + w_z = 0, \tag{2.3}$$

$$\boldsymbol{u}_t + \varepsilon \boldsymbol{u} \cdot \nabla \boldsymbol{u} + \frac{\varepsilon}{\mu^2} w \boldsymbol{u}_z = -\nabla p, \tag{2.4}$$

$$\varepsilon w_t + \varepsilon^2 \boldsymbol{u} \cdot \nabla w + \frac{\varepsilon^2}{\mu^2} w w_z = -\varepsilon p_z - 1, \tag{2.5}$$

where $\boldsymbol{u} = (u, v)$ denotes the horizontal velocity vector, $\nabla = (\partial/\partial x, \partial/\partial y)$ the horizontal gradient vector, and the subscript the partial derivative.

On the free surface, $z = \varepsilon\zeta(x, y, t)$, the usual kinematic and dynamic boundary conditions apply,

$$w = \mu^2(\zeta_t + \varepsilon\boldsymbol{u} \cdot \nabla\zeta) \quad \text{on } z = \varepsilon\zeta, \tag{2.6 a}$$

$$p = 0. \tag{2.6 b}$$

Along the seafloor, $z = -h$, the kinematic boundary condition requires

$$w + \mu^2\boldsymbol{u} \cdot \nabla h + \frac{\mu^2}{\varepsilon}h_t = 0 \quad \text{on } z = -h. \tag{2.7}$$

For later use, we note here that the depth-integrated continuity equation can be obtained by integrating (2.3) from $z = -h$ to $z = \varepsilon\zeta$. After applying the boundary conditions (2.6), the resulting equation reads

$$\nabla \cdot \left[\int_{-h}^{\varepsilon\zeta} \boldsymbol{u}\,\mathrm{d}z\right] + \frac{1}{\varepsilon}H_t = 0, \tag{2.8}$$

where

$$H = \varepsilon\zeta + h. \tag{2.9}$$

We remark here that (2.8) is exact.

3. Approximate two-dimensional governing equations

The three-dimensional boundary-value problem described in the previous section will be approximated and projected onto a two-dimensional horizontal plane. In this section, the nonlinearity is assumed to be of $O(1)$. However, the frequency dispersion is assumed to be weak, i.e.

$$O(\mu^2) \ll 1. \tag{3.1}$$

Using μ^2 as the small parameter, a perturbation analysis is performed on the primitive governing equations. The complete derivation is given in Appendix A. The resulting approximate continuity equation is

$$\frac{1}{\varepsilon}h_t + \zeta_t + \nabla \cdot (H\boldsymbol{u}_\alpha)$$
$$- \mu^2\nabla \cdot \left\{H\left[(\tfrac{1}{6}(\varepsilon^2\zeta^2 - \varepsilon\zeta h + h^2) - \tfrac{1}{2}z_\alpha^2)\nabla(\nabla \cdot \boldsymbol{u}_\alpha)\right.\right.$$
$$\left.\left. + (\tfrac{1}{2}(\varepsilon\zeta - h) - z_\alpha)\nabla\left(\nabla \cdot (h\boldsymbol{u}_\alpha) + \frac{h_t}{\varepsilon}\right)\right]\right\} = O(\mu^4). \tag{3.2}$$

Equation (3.2) is one of three governing equations for ζ and $\boldsymbol{u}_\alpha$. The other two equations come from the horizontal momentum equation (2.4) and are given in vector

form as

$$\boldsymbol{u}_{\alpha t} + \varepsilon \boldsymbol{u}_\alpha \cdot \nabla \boldsymbol{u}_\alpha + \nabla \zeta$$
$$+ \mu^2 \frac{\partial}{\partial t} \left\{ \tfrac{1}{2} z_\alpha^2 \nabla (\nabla \cdot \boldsymbol{u}_\alpha) + z_\alpha \nabla \left[\nabla \cdot (h\boldsymbol{u}_\alpha) + \frac{h_t}{\varepsilon} \right] \right\}$$
$$+ \varepsilon \mu^2 \left\{ \left[\nabla \cdot (h\boldsymbol{u}_\alpha) + \frac{h_t}{\varepsilon} \right] \nabla \left[\nabla \cdot (h\boldsymbol{u}_\alpha) + \frac{h_t}{\varepsilon} \right] \right.$$
$$- \nabla \left[\zeta \left(\nabla \cdot (h\boldsymbol{u}_\alpha)_t + \frac{h_{tt}}{\varepsilon} \right) \right] + (\boldsymbol{u}_\alpha \cdot \nabla z_\alpha) \nabla \left[\nabla \cdot (h\boldsymbol{u}_\alpha) + \frac{h_t}{\varepsilon} \right]$$
$$+ z_\alpha \nabla \left[\boldsymbol{u}_\alpha \cdot \nabla \left(\nabla \cdot (h\boldsymbol{u}_\alpha) + \frac{h_t}{\varepsilon} \right) \right] + z_\alpha (\boldsymbol{u}_\alpha \cdot \nabla z_\alpha) \nabla (\nabla \cdot \boldsymbol{u}_\alpha)$$
$$\left. + \tfrac{1}{2} z_\alpha^2 \nabla [\boldsymbol{u}_\alpha \cdot \nabla (\nabla \cdot \boldsymbol{u}_\alpha)] \right\}$$
$$+ \varepsilon^2 \mu^2 \nabla \left\{ -\tfrac{1}{2} \zeta^2 \nabla \cdot \boldsymbol{u}_{\alpha t} - \zeta \boldsymbol{u}_\alpha \cdot \nabla \left[\nabla \cdot (h\boldsymbol{u}_\alpha) + \frac{h_t}{\varepsilon} \right] + \zeta \left[\nabla \cdot (h\boldsymbol{u}_\alpha) + \frac{h_t}{\varepsilon} \right] \nabla \cdot \boldsymbol{u}_\alpha \right\}$$
$$+ \varepsilon^3 \mu^2 \nabla \{ \tfrac{1}{2} \zeta^2 [(\nabla \cdot \boldsymbol{u}_\alpha)^2 - \boldsymbol{u}_\alpha \cdot \nabla (\nabla \cdot \boldsymbol{u}_\alpha)] \} = O(\mu^4). \tag{3.3}$$

Equations (3.2) and (3.3) are the coupled governing equations, written in terms of $\boldsymbol{u}_\alpha$ and ζ, for fully nonlinear weakly dispersive waves generated by a seafloor movement. We reiterate here that $\boldsymbol{u}_\alpha$ is evaluated at $z = z_\alpha(x, y, t)$, which is a function of time. The choice of z_α is made based on the linear frequency-dispersion characteristics of the governing equations (e.g. Nwogu 1993; Chen & Liu 1995). Assuming a stationary seafloor, in order to extend the applicability of the governing equations to relatively deep water (or a short wave), z_α is recommended to be evaluated as $z_\alpha = -0.531h$. In the following analysis, the same relationship is employed. These model equations will be referred to as FNL-EXT, for fully nonlinear 'extended' equations.

Up to this point, the time-scale of the seafloor movement is assumed to be in the same order of magnitude as the typical period of generated water wave, $t_{\mathrm{w}} = \ell_0 / \sqrt{gh_0}$ as given in (2.1). When the ground movement is creeping in nature, the time-scale of seafloor movement, t_{c}, could be larger than t_{w}. The only scaling parameter that is directly affected by the time-scale of the seafloor movement is the characteristic amplitude of the wave motion. After introducing the time-scale t_{c} into the time derivatives of h in the continuity equation (3.2), along with a characteristic change in water depth Δh, the coefficient in front of h_t becomes

$$\frac{\delta}{\varepsilon} \frac{t_{\mathrm{w}}}{t_{\mathrm{c}}},$$

where $\delta = \Delta h / h_0$. To maintain the conservation of mass, the above parameter must be of order one. Thus

$$\varepsilon = \delta \frac{t_{\mathrm{w}}}{t_{\mathrm{c}}} = \frac{\delta l_0}{t_{\mathrm{c}} \sqrt{gh_0}}. \tag{3.4}$$

The above relationship can be interpreted in the following way. During the creeping ground movement, over the time period $t < t_{\mathrm{c}}$ the generated wave has propagated a distance $t\sqrt{gh_0}$. The total volume of the seafloor displacement, normalized by h_0, is $\delta l_0(t/t_{\mathrm{c}})$, which should be the same as the volume of water underneath the generated

wave crest, i.e. $\varepsilon t \sqrt{gh_0}$. Therefore, over the ground-movement period, $t < t_c$, the wave amplitude can be estimated by (3.4). Consequently, nonlinear effects become important only if ε defined in (3.4) is $O(1)$. Since, by the definition of a creeping slide, the value $l_0/(t_c \sqrt{gh_0})$ is always less than one, fully nonlinear effects will be important for only the largest slides. The same conclusion was reached by Hammack (1973), using a different approach. The importance of the fully nonlinear effect when modelling creeping ground movements will be tested in §8.

4. Limiting cases

In this section, the general model is further simplified for different physical conditions.

(a) Weakly nonlinear waves

In many situations, the seafloor displacement is relatively small in comparison with the local depth, and the seafloor movement can be approximated as

$$h(x, y, t) = h_0(x, y) + \delta \bar{h}(x, y, t), \tag{4.1}$$

in which δ is considered to be small. In other words, the maximum seafloor displacement is much smaller than the characteristic water depth. Since the free-surface displacement is directly proportional to the seafloor displacement, i.e. $O(\varepsilon \zeta) = O(\delta \bar{h})$, or much less than the seafloor displacement in the case of creeping ground movements, we can further simplify the governing equations derived in the previous section by allowing

$$O(\varepsilon) = O(\delta) = O(\mu^2) \ll 1, \tag{4.2}$$

which is the Boussinesq approximation. Thus the continuity equation (3.2) can be reduced to

$$\zeta_t + \nabla \cdot (H\boldsymbol{u}_\alpha) + \frac{\delta}{\varepsilon} \bar{h}_t$$
$$- \mu^2 \nabla \cdot \left\{ h_0 \left[(\tfrac{1}{6}h_0^2 - \tfrac{1}{2}z_\alpha^2)\nabla(\nabla \cdot \boldsymbol{u}_\alpha) - (\tfrac{1}{2}h_0 + z_\alpha)\nabla \left(\nabla \cdot (h_0 \boldsymbol{u}_\alpha) + \frac{\delta}{\varepsilon}\bar{h}_t \right) \right] \right\}$$
$$= O(\mu^4, \mu^2 \varepsilon, \delta \mu^2). \tag{4.3}$$

The momentum equation becomes

$$\boldsymbol{u}_{\alpha t} + \varepsilon \boldsymbol{u}_\alpha \cdot \nabla \boldsymbol{u}_\alpha + \nabla \zeta + \mu^2 \frac{\partial}{\partial t} \left\{ \tfrac{1}{2}z_\alpha^2 \nabla(\nabla \cdot \boldsymbol{u}_\alpha) + z_\alpha \nabla \left[\nabla \cdot (h_0 \boldsymbol{u}_\alpha) + \frac{\delta}{\varepsilon}\bar{h}_t \right] \right\}$$
$$= O(\mu^4, \varepsilon \mu^2, \delta \mu^2). \tag{4.4}$$

These model equations will be referred to as WNL-EXT, for weakly nonlinear 'extended' equations. The linear version of the above will also be used in the following analysis, and will be referred to as L-EXT, for linear 'extended' equations.

It is also possible to express the approximate continuity and momentum equations in terms of a depth-averaged velocity. The depth-averaged equations can be derived using the same method presented in Appendix A. One version of the depth-averaged

equations will be employed in future sections, which is subject to the restraint (4.2), and is given as

$$\zeta_t + \nabla \cdot (H\bar{\boldsymbol{u}}) + \frac{\delta}{\varepsilon}\bar{h}_t = 0 \tag{4.5}$$

and

$$\bar{\boldsymbol{u}}_t + \varepsilon\bar{\boldsymbol{u}} \cdot \nabla\bar{\boldsymbol{u}} + \nabla\zeta + \mu^2\frac{\partial}{\partial t}\left\{\tfrac{1}{2}h_0^2\nabla(\nabla \cdot \bar{\boldsymbol{u}}) - \tfrac{1}{6}h_0\nabla\left[\nabla \cdot (h_0\bar{\boldsymbol{u}}) + \frac{\delta}{\varepsilon}\bar{h}_t\right]\right\}$$
$$= O(\mu^4, \varepsilon\mu^2, \delta\mu^2), \tag{4.6}$$

where the depth-averaged velocity is defined as

$$\bar{\boldsymbol{u}}(x, y, t) = \frac{1}{h + \varepsilon\zeta}\int_h^{\varepsilon\zeta} \boldsymbol{u}(x, y, z, t)\,\mathrm{d}z. \tag{4.7}$$

This set of model equations (4.5) and (4.6) will be referred to as WNL-DA, for weakly nonlinear depth-averaged equations.

(*b*) *Nonlinear shallow-water waves*

In the case that the water depth is very shallow or the wavelength is very long, the governing equations (3.2) and (3.3) can be truncated at $O(\mu^2)$. These resulting equations are the well-known nonlinear shallow-water equations in which the seafloor movement is the forcing term for wave generation. This set of equations will be referred to as NL-SW, for nonlinear shallow-water equations.

5. Numerical model

In this paper, a finite-difference algorithm is presented for the general model equations, FNL-EXT. This model has the robustness of enabling slide-generated surface waves, although initially linear or weakly nonlinear in nature, to propagate into shallow water, where fully nonlinear effects may become important. The algorithm is developed for the general two-horizontal-dimension problem; however, in this paper, only one-horizontal-dimension examples are examined. The structure of the present numerical model is similar to those of Wei & Kirby (1995) and Wei *et al.* (1995). Differences between the model presented here and that of Wei *et al.* exist in the added terms due to a time-dependent water depth and the numerical treatment of some nonlinear-dispersive terms, which is discussed in more detail in Appendix B. A high-order predictor-corrector scheme is used, employing a third order in time explicit Adams–Bashforth predictor step, and a fourth order in time Adams–Moulton implicit corrector step (Press *et al.* 1989). The implicit corrector step must be iterated until a convergence criterion is satisfied. All spatial derivatives are differenced to fourth-order accuracy, yielding a model that is numerically accurate to $(\Delta x)^4$, $(\Delta y)^4$ in space and $(\Delta t)^4$ in time. The governing equations (3.2) and (3.3) are dimensionalized for the numerical model, and all variables described in this and following sections will be in the dimensional form. Note that the dimensional equations are equivalent to the non-dimensional ones with $\varepsilon = \mu = 1$ and the addition of gravity, g, to the coefficient of the leading-order free-surface derivative in the momentum equation (i.e. the third term on the left-hand side of (3.3)). The predictor-corrector

equations are given in Appendix B, along with some additional description of the numerical scheme. Run-up and rundown of the waves generated by the submarine disturbance will also be examined. The moving-boundary scheme employed here is the technique developed by Lynett *et al.* (2002). Founded around the restrictions of the high-order numerical wave-propagation model, the moving-boundary scheme uses linear extrapolation of free surface and velocity through the shoreline, into the dry region. This approach allows for the five-point finite-difference formulae to be applied at all points, even those neighbouring dry points, and thus eliminates the need of conditional statements.

In addition to the depth-integrated-model numerical results, output from a two-dimensional (vertical-plane) BIEM model will be presented for certain cases. This BIEM model will be primarily used to determine the deep-water-accuracy limit of the depth-integrated model. The BIEM model solves for inviscid irrotational flows and converts a boundary-value problem into an integral equation along the boundary of a physical domain. Therefore, just as with the depth-integration approach, it reduces the dimension of the problem by one. The BIEM model used here solves the Laplace equation in the vertical plane (x, z), and, of course, is valid in all water depths for all wavelengths. Details of this type of BIEM model, when used to model water-wave propagation, can be found in Grilli *et al.* (1989), Liu *et al.* (1992) and Grilli (1993), for example. The BIEM model used in this work has reproduced the numerical results presented for landslide-generated waves in Grilli & Watts (1999) perfectly.

6. Comparisons with experiment and other models

As a first check of the present model, a comparison between Hammack's (1973) experimental data for an impulsive bottom movement in a constant water depth is made. The bottom movement consists of a length, $l_0 = 24.4$ water depths, which is pushed vertically upward. The change in depth for this experiment, δ, is 0.1, so nonlinear effects should play a small role near the source region. Figure 2 shows a comparison between the numerical results using FNL-EXT, experimental data and the linear theory presented by Hammack. Both the fully nonlinear model and the linear theory agree well with experiment at the edge of the source region (figure 2a). From figure 2b, a time-series taken at 20 water depths from the edge of the source region, the agreement between all data is again quite good, but the deviation between the linear theory and experiment is slowly growing. The purpose of this comparison is to show that the present numerical model accurately predicts the free-surface response to a simple seafloor movement. It would seem that if one was interested in just the wave field very near the source, linear theory is adequate. However, as the magnitude of the bed upthrust, δ, becomes large, linear theory is not capable of accurately predicting the free-surface response, even very near the source region. One such linear versus nonlinear comparison is shown in figure 2 for $\delta = 0.6$. The motion of the bottom movement is the same as in Hammack's case above. Immediately on the outskirts of the bottom movement, there are substantial differences between linear and nonlinear theory, as shown in figure 2c. Additionally, as the wave propagates away from the source, errors in linear theory are more evident.

A handful of experimental trials and analytic solutions exist for non-impulsive seafloor movements. However, for the previous work that made use of smooth obstacles, such as a semicircle (e.g. Forbes & Schwartz 1982) or a semi-ellipse (e.g. Lee *et*
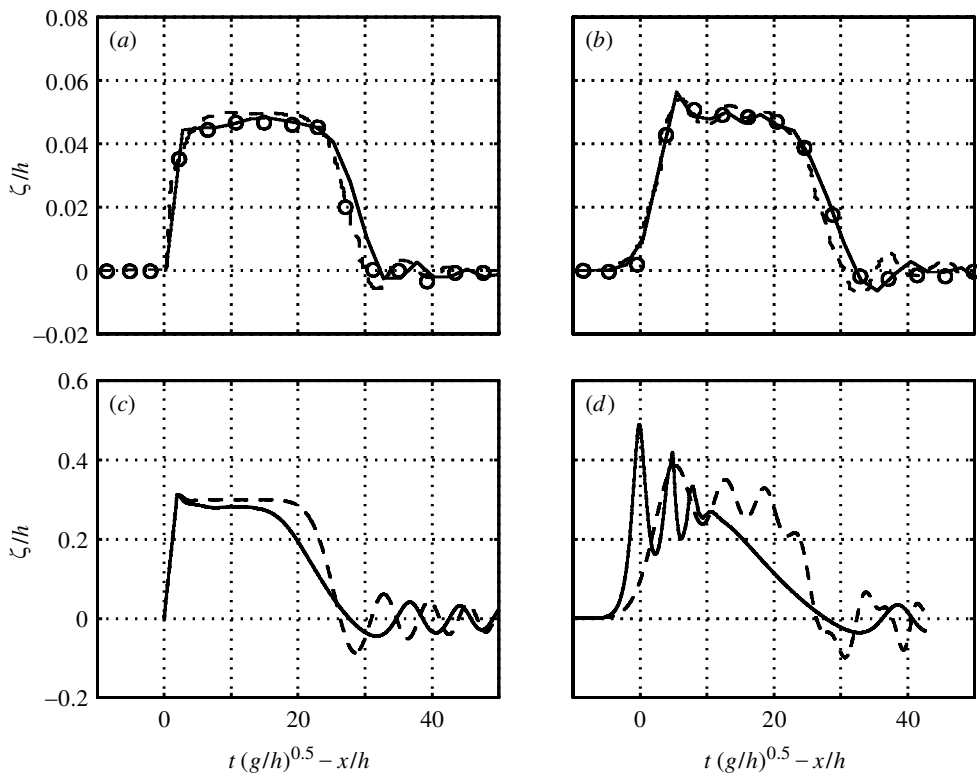
Figure 2. (*a*), (*b*) Comparison between Hammack's (1973) experimental data (dots) for an impulsive seafloor upthrust of $\delta = 0.1$, FNL-EXT numerical simulation (solid line), and linear theory (dashed line). (*a*) Time-series at $x/h = 0$; (*b*) time-series at $x/h = 20$, where x is the distance from the edge of the impulsive movement. (*c*), (*d*) FNL-EXT (solid line) and L-EXT (dashed line) numerical results for Hammack's set-up, except with $\delta = 0.6$.

al. 1989), the length of the obstacle is always less than 1.25 water depths, or $\mu \geqslant 0.8$. Unfortunately, these objects will create waves too short to be modelled accurately by a depth-integrated model.

Watts (1997) performed a set of experiments where he let a triangular block free fall down a planar slope. In all the experiments, the front (deep-water) face of the block was steep, and in some cases vertical. Physically, as the block travels down a slope, water is pushed out horizontally from the vertical front. Numerically, however, using the depth-integrated model, the dominant direction of water motion near the vertical face is vertical. This can be explained as follows. Examining the depth-integrated-model equations, starting from the leading-order shallow-water-wave equations, the only forcing term due to the changing water depth appears in the continuity equation. There is no forcing term in the horizontal momentum equation. Therefore, in the non-dispersive system, any seafloor bottom cannot directly create a horizontal velocity. This concept can be further illuminated by the equation describing the vertical profile of horizontal velocity,

$$\boldsymbol{u}(x, y, z, t) = \boldsymbol{u}_\alpha(x, y, t) + O(\mu^2). \tag{6.1}$$
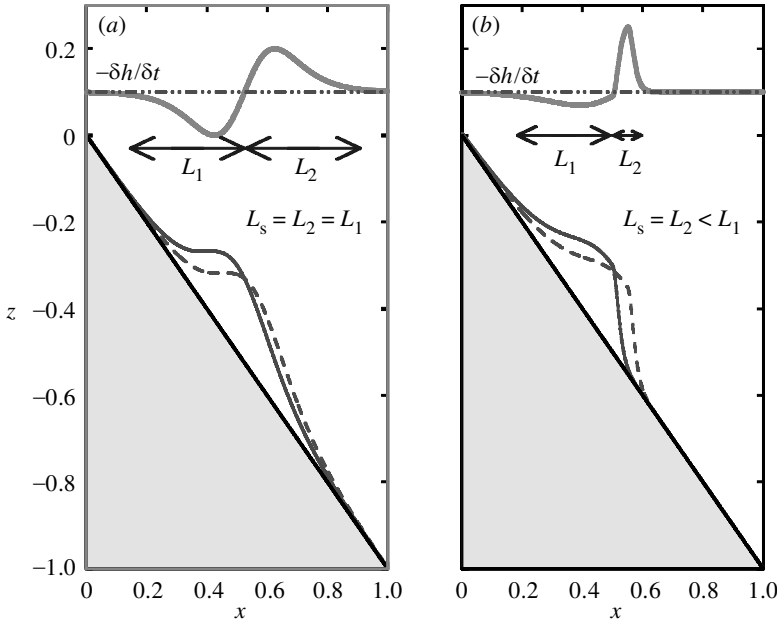
Figure 3. Graphical definition of the characteristic side length of a slide mass. The slide mass at time t_0 is shown by the solid line, while the profile at some time $t > t_0$ is shown by the dashed line. The negative of the change in water depth (or the approximate free-surface response in the non-dispersive equation model) during the increment $t - t_0$ is shown by the thick line plotted on $z = 0.1$.

Again, the changing seafloor bottom cannot directly create a horizontal velocity component for the non-dispersive system. All of the seafloor movement, whether it is a vertical or translational motion, is interpreted as strictly a vertical motion, which can lead to a very different generated wave pattern.

When adding the weakly dispersive terms, the vertical profile of the horizontal velocity becomes

$$\boldsymbol{u}(x,y,z,t) = \boldsymbol{u}_\alpha(x,y,t) - \mu^2 \left\{ \tfrac{1}{2}z^2 - z_\alpha^2 \nabla(\nabla \cdot \boldsymbol{u}_\alpha) + (z - z_\alpha)\nabla\left[\nabla \cdot (h\boldsymbol{u}_\alpha) + \frac{h_t}{\varepsilon}\right]\right\} + O(\mu^4).$$
(6.2)

Now, with the higher-order dispersive formulation, there is the forcing term, ∇h_t, which accounts for the effects of a horizontally moving body. Keep in mind, however, that this forcing term is a second-order correction, and therefore should represent only a small correction to the horizontal velocity profile. Thus, with rapid translational motion and/or steep side slopes of a submarine slide, the flow motion is strongly horizontal locally, and the depth-integrated models are not adequate. In slightly different terms, let the slide mass have a characteristic side length, L_s. A side length is defined as the horizontal distance between two points at which $\partial h/\partial t = 0$. This definition of a side length is described graphically in figure 3. Figure 3a shows a slide mass that is symmetric around its midpoint in the horizontal direction, where the back (shallow-water) and front (deep-water) side lengths are equal. Figure 3b shows a slide mass whose front side is much shorter that the back. Note that for the slide shown in figure 3b, the side lengths, measured in the
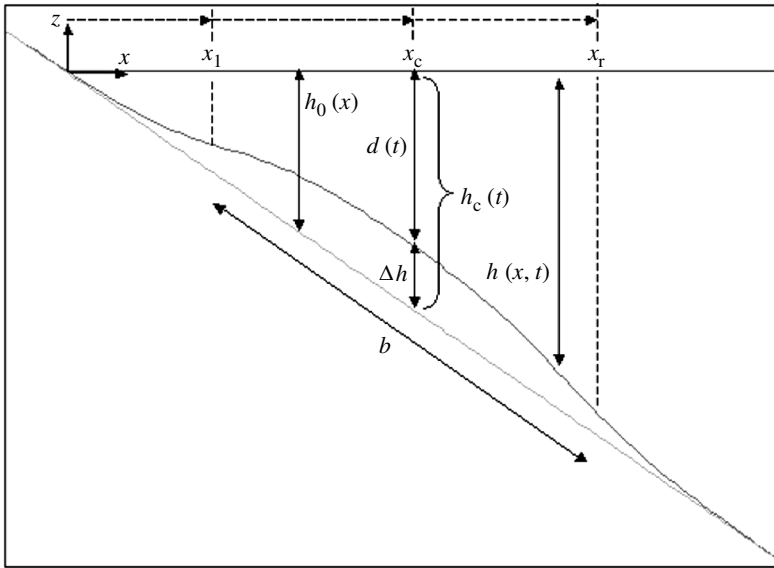
Figure 4. Set-up for submarine landslide comparisons.

direction parallel to the slope, are equal, whereas for the slide in figure $3a$, the slide lengths are equal when measured in the horizontal direction. An irregular slide mass will have at least two different side lengths. In these cases, the characteristic side length, L_s, is the shortest of all sides. When L_s is small compared to a characteristic water depth, h_0, that side is considered steep, or in deep water, and the shallow-water-based depth-integrated model will not be accurate. For the vertical face of Watts's experiments, $L_s = 0$, and therefore $L_s/h_0 = 0$, and the situation resembles that of an infinitely deep ocean. The next section will attempt to determine a limiting value of L_s/h_0 where the depth-integrated model begins to fail.

7. Limitations of the depth-integrated model

Before using the model for practical applications, the limits of accuracy of the depth-integrated model must be determined. As illustrated above, just as there is a short-wave accuracy limit (wave should be at least two water depths long when applying the 'extended' model), it is expected that there is also a slide length-scale limitation. By comparing the outputs of this model to those of the BIEM model, a limiting value of L_s/h_0 can be inferred. The high degree of BIEM model accuracy in simulating wave propagation is well documented (e.g. Grilli 1993; Grilli *et al.* 1995).

The comparison cases will use a slide mass travelling down a constant slope. The slide mass moves as a solid body, with velocity described following Watts (1997). This motion is characterized by a decreasing acceleration until a terminal velocity is reached. All of the solid-body motion coefficients used in this paper are identical to those employed by Grilli & Watts (1999). Note that all of the submarine landslide simulations presented in this paper are non-breaking.
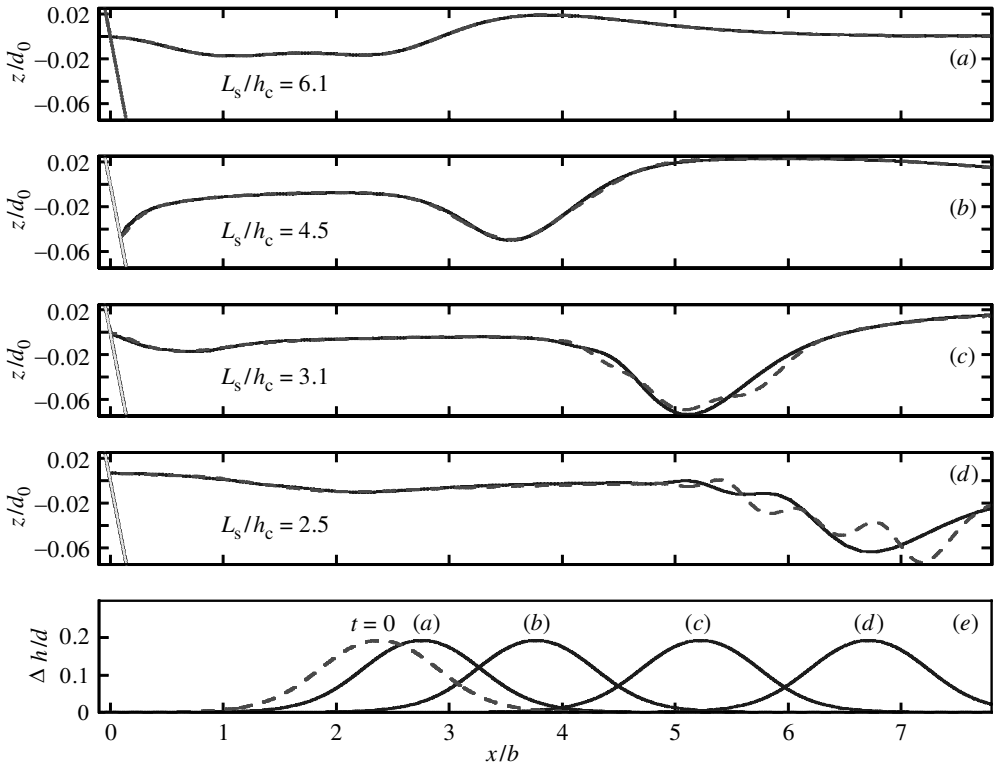
Figure 5. Free-surface snapshots for BIEM (solid line) and depth-integrated (dashed line) results at $t(g/d_0)^{1/2}$ values of (a) 10.6, (b) 21, (c) 31.6 and (d) 41. (e) The location of the slide mass in each of the four snapshots above.

The set-up of the slide mass on the slope is shown in figure 4. The time-history of the seafloor is described by

$$h(x,t) = h_0(x) - \tfrac{1}{2}\Delta h \left[1 + \tanh\left(\frac{x - x_1(t)}{S}\right)\right]\left[1 - \tanh\left(\frac{x - x_r(t)}{S}\right)\right], \qquad (7.1)$$

where Δh is the maximum vertical height of the slide, x_1 is the location of the tanh inflection point of the left side of the slide, x_r is the location of the inflection point on the right side, and S is a shape factor, controlling the steepness of the slide sides. The left and right boundaries and steepness factor are given by

$$x_1(t) = x_c(t) - \tfrac{1}{2}b\cos(\theta), \qquad x_r(t) = x_c(t) + \tfrac{1}{2}b\cos(\theta), \qquad S = \frac{0.5}{\cos(\theta)},$$

where x_c is the horizontal location of the centre point of the slide, and is determined using the equations governing the solid body motion of the slide. The angle of the slope is given by θ. The thickness of the 'slideless' water column, or the baseline water depth, at the centre point of the slide is defined by $h_c(t) = h_0(x_c(t)) = \Delta h + d(t)$. With a specified depth above the initial centre point of the slide mass, $d_0 = d(t = 0)$, the initial horizontal location of the slide centre, $x_c(t = 0)$, can be found. The length along the slope between x_1 and x_r is defined as b, and all lengths are scaled by b.
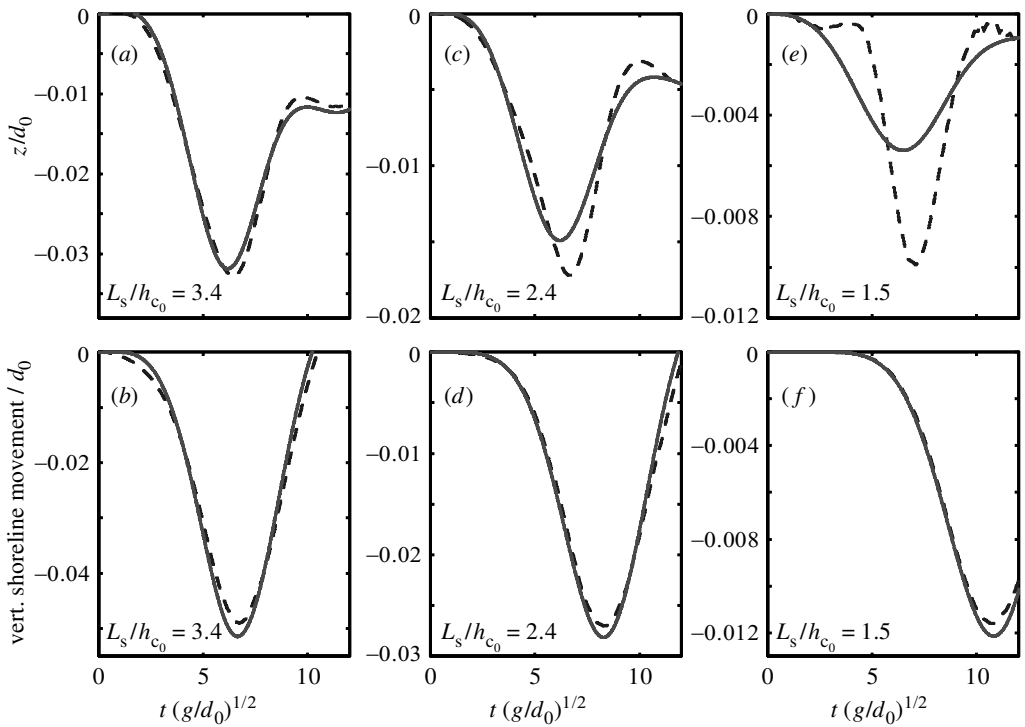
Figure 6. Time-series above the initial centre point of the slide ((a), (c), (e)) and vertical movement of the shoreline ((b), (d), (f)) for a $20°$ slope and a slide mass with a maximum height $\Delta h = 0.1$. BIEM results are shown by the solid line, depth-integrated results by the dashed line. (a), (b) $d_0/b = 0.4$; (c), (d) $d_0/b = 0.6$; and (e), (f) $d_0/b = 1.0$.

For the first comparison, a slide with the parameter set $\theta = 6°$, $d_0/b = 0.2$ and $\Delta h/b = 0.05$ is modelled with FNL-EXT and BIEM. With these parameters, the characteristic horizontal side length of the slide mass, L_s/b, is 1.7. L_s is defined as in figure 3 or, specifically, the horizontal distance between two points at which $\partial h/\partial t$ is less than 1% of the maximum $\partial h/\partial t$ value. Note that a $6°$ slope is roughly $\frac{1}{10}$. Figure 5 shows four snapshots of the free-surface elevation from both models. The lowest panel in the figure shows the initial location of the slide mass, along with the locations corresponding to the four free-surface snapshots. Initially, as shown in figure 5a,b, where $L_s/h_c = 6.1$ and 4.5 respectively, the two models agree, and thus are still in the range of acceptable accuracy of the depth-integrated model. In figure 5c, as the slide moves into deeper water, where $L_s/h_c = 3.1$, the two models begin to diverge over the source region, and by figure 5d, the free-surface responses of the two models are quite different. These results indicate that in the vicinity of $x/b = 5$, the depth-integrated model becomes inaccurate. At this location, $h_c/b = 0.5$ and $L_s/h_c = 3.4$.

Numerous additional comparison tests were performed, and all indicated that the depth-integrated model becomes inaccurate when $L_s/h_c < 3$–3.5. One more of the comparisons is shown here. Examining a $20°$ slope and a slide mass with a maximum height $\Delta h/b = 0.1$, the initial depth of submergence, d_0/b, will be successively increased from 0.4 to 0.6 to 1.0. The corresponding initial L_s/h_c values are 3.4, 2.4

and 1.5, respectively. Time-series above the initial centre point of the slide masses and vertical shoreline movements are shown in figure 6. The expectation is that the first case ($L_s/h_c = 3.4$ initially) should show good agreement, the middle case ($L_s/h_c = 2.4$ initially) marginal agreement, and the last case ($L_s/h_c = 1.5$ initially) bad agreement. The time-series above the centre, figure 6*a, c, e*, clearly agree with the stated expectation. Various different z_α levels were tested in an attempt to better the agreement with the BIEM-model results for the deeper water cases, but $z_\alpha = -0.531h$ provided the most accurate output. Rundown, as shown in figure 6*b, d, f*, shows good agreement for all the trials. The explanation is that the wave that creates the rundown is generated from the back face of the slide mass. This wave sees a characteristic water depth that is less than h_c, and thus this back face wave remains in the region of accuracy of the depth-integrated model, whereas the wave motion nearer to the front face of the slide is inaccurate. This feature is also clearly shown in figure 5. Thus, if one was solely interested in the leading wave approaching the shoreline, the characteristic water depth should be interpreted as the average depth along the back face of the slide, instead of h_c. The inaccurate elevation waves created by the front face of the moving mass could be absorbed numerically, such as with a sponge layer, so that they do not effect the simulation.

A guideline that the depth-integrated 'extended' model will yield accurate results for $L_s/h_c > 3.5$ is accepted. This restriction would seem to be more stringent than the 'extended' model frequency-dispersion limitation, which requires that the free-surface wave be at least two water depths long. In fact, the slide length-scale limitation is more in line with the dispersion limitations of the depth-averaged (conventional) model. The limitations of the various model formulations, i.e. 'extended' and depth averaged, are discussed in the next section.

8. Importance of nonlinearity and frequency dispersion

Another useful guideline would be to know when nonlinear effects begin to play an important role. This can be determined by running numerous numerical trials, employing the FNL-EXT, WNL-EXT and L-EXT equation models. These three equation sets share identical linear-dispersion properties, but have varying levels of nonlinearity. The linear-dispersion limit of these 'extended' equations, for the rigid bottom case, is near $kh = 3$, where k is the wavenumber. Nonlinearity, however, is only faithfully captured to near $kh = 1.0$ for the FNL-EXT model, and to an even lesser value for WNL-EXT (Gobbi *et al.* 2000). The source-generation accuracy limitation of the model is such that the side length of the landslide over the depth must be greater than 3.5. If the slide is symmetric in the horizontal direction, which is the only type of slide examined in this section, then the wavelength of the generated wave will be $2 \times 3.5 \times h$, or roughly $kh = 1$. Thus, up to the accuracy limit found in the previous section, nonlinearity is expected to be well captured. The FNL-EXT model will be considered correct, and any difference in output compared to the other models with lesser nonlinearity would indicate that full nonlinear effects are important.

The importance of nonlinearity will be tested through examination of various $\Delta h/d_0$ combinations, using the slide mass described in the previous section. The value of $\Delta h/d_0$ can be thought of as an impulsive nonlinearity, as this value represents the magnitude of the free-surface response if the slide motion was entirely vertical and instantaneous. The procedure will be to hold the value $h_{c_0} = h_c(t = 0) = \Delta h + d_0$
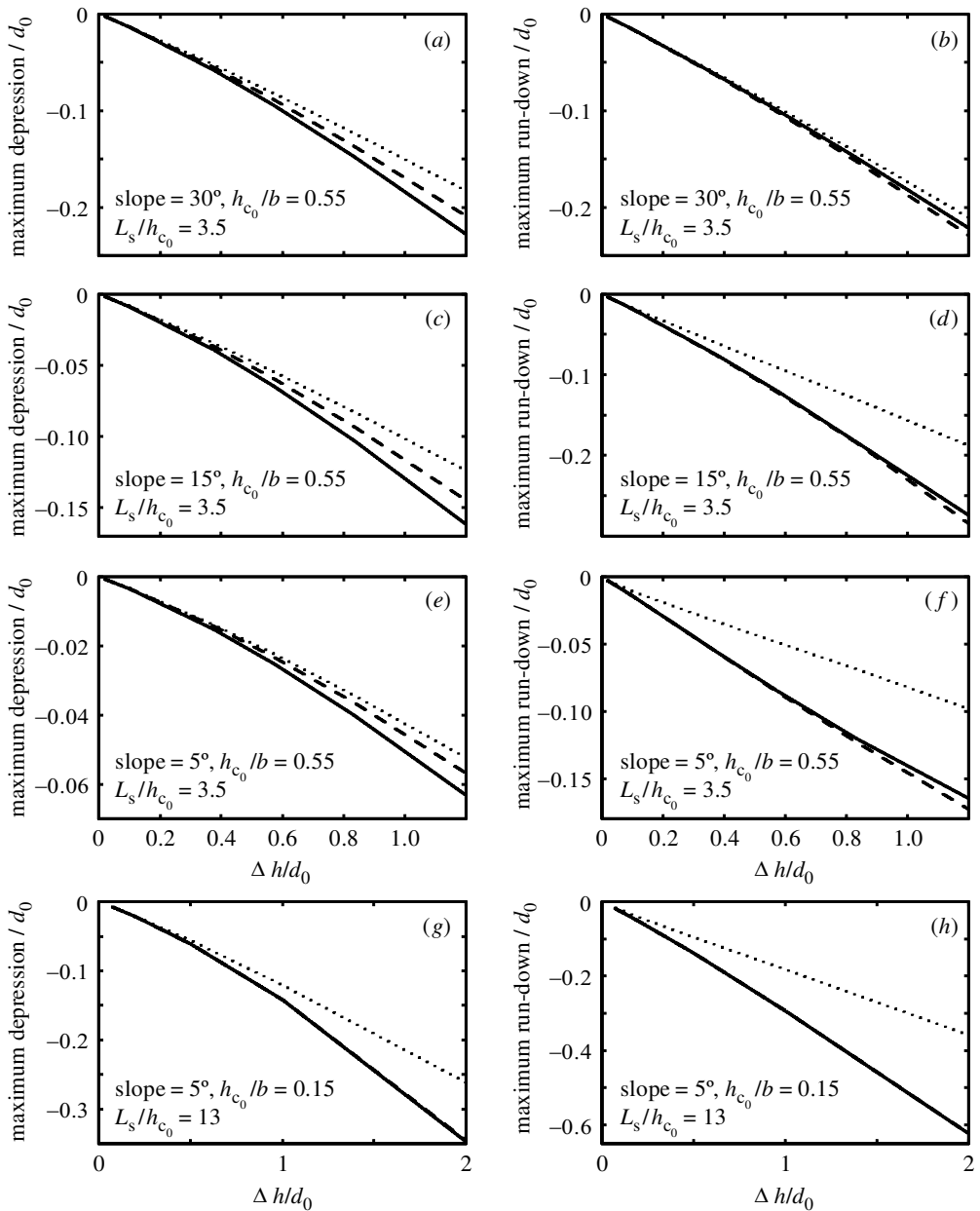
Figure 7. Maximum depression above the initial centre point of the slide mass and maximum rundown for four different trial sets. FNL-EXT results indicated by the solid line, WNL-EXT by the dashed line and L-EXT by the dotted line.

constant for a given slope angle, while altering Δh and d_0. Two output values will be compared between all the simulations: maximum depression above the initial centre point of the slide and maximum rundown. For all simulations presented in this section, $\Delta x/b = 0.003$ and $\Delta t\sqrt{gh_{c_0}}/b = 0.0003$.

Table 1. *Characteristics of the simulations performed for the nonlinearity test*

set no.	slope (deg)	h_{c_0}/b	L_s/h_{c_0}
1	30	0.55	3.5
2	15	0.55	3.5
3	5	0.55	3.5
4	5	0.15	13

Figure 7 shows the output from four sets of comparisons, whose characteristics are given in table 1. Figure $7a, b$ show the depression above the centre point and the rundown for set 1, figure $7c, d$ for set 2, figure $7e, f$ for set 3 and figure $7g, h$ for set 4. Examining the maximum depression plots for sets 1–3, it is clear that the trends between the three sets are very similar, with FNL-EXT predicting the largest depression and L-EXT predicting the smallest. The difference between FNL-EXT and WNL-EXT is solely due to nonlinear-dispersive terms, which are of $O(\varepsilon\mu^2)$, while the difference between WNL-EXT and L-EXT is caused by the nonlinear-divergence term in the continuity equation and the convection term in the momentum equation, which are of $O(\varepsilon)$. The relative differences in the maximum depression predicted between FNL-EXT and WNL-EXT are roughly the same as the differences between WNL-EXT and L-EXT for sets 1, 2 and 3. Therefore, in the source region, for L_s/h_{c_0} values near the accuracy limit of the 'extended' model (near 3.5), the nonlinear-dispersive terms are as necessary to include in the model as the leading order nonlinear terms. As the L_s/h_c value is increased, the slide produces an increasingly longer (shallow-water) wave. Frequency dispersion plays a lesser role, and thus the nonlinear-dispersive terms become expectedly less important. This can be seen in the maximum depression plot for set 4. For this set, $L_s/h_{c_0} = 13$, and the FNL-EXT and WNL-EXT results are nearly indistinguishable.

Inspecting the maximum rundown plots for sets 1, 2 and 3, it seems that the trends between the three different models have changed. Now, WNL-EXT predicts the largest rundown, while L-EXT predicts the smallest. It is hypothesized that the documented over-shoaling of WNL-EXT (Wei *et al.* 1995) cancels out the lesser wave height generated in the source region compared to FNL-EXT, leading to rundown heights that agree well between the two models. As the slope is decreased, the error in the L-EXT rundown prediction increases. This is attributed to a longer distance of shoaling before the wave reaches the shoreline. As the slope is decreased, while h_{c_0} is kept constant, the horizontal distance from the shoreline to the initial centre point of the slide increases. The slide length is roughly the same for the three sets, therefore the generated wavelength is roughly the same. Thus, with a lesser slope, the generated wave shoals for a greater number of wave periods. During this relatively larger distance of shoaling, nonlinear effects, and in particular the leading-order nonlinear effects, accumulate and yield large errors in the linear (L-EXT) simulations. This trend is also evident in the rundown plot for set 4. Also note that in set 4, where the nonlinear-dispersive terms are very small, the FNL-EXT and WNL-EXT rundowns are identical.
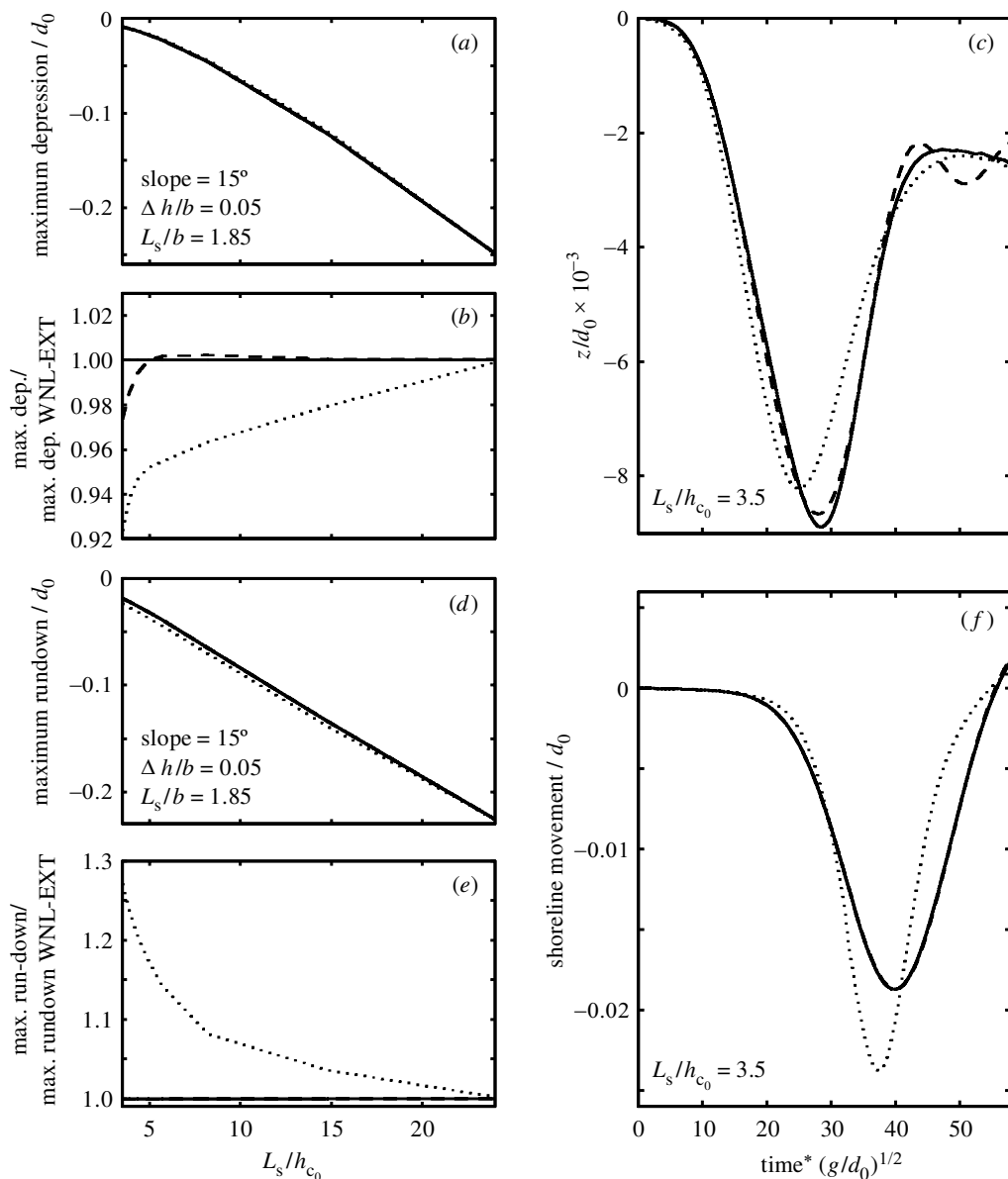
Figure 8. Maximum depression above the initial centre point of the slide mass (*a*) and maximum rundown (*d*) for a set of numerical simulations on a $15°$ slope. (*b*), (*e*) The maximum depression and maximum rundown scaled by the corresponding values from the WNL-EXT model. Time-series comparisons for $L_s/h_{c_0} = 3.5$ showing the free-surface elevation above the centre point (*c*) and vertical shoreline movement (*f*) are given on the right. WNL-EXT results indicated by the solid line, WNL-DA by the dashed line and NL-SW by the dotted line.

A deep-water limit has been determined for the 'extended' model ($L_s/h_c > 3.5$), but it would also be interesting to know the limits of applicability of the depth-averaged (WNL-DA) and shallow-water (NL-SW) models. The only differences

between these three models (the weakly nonlinear 'extended', weakly nonlinear depth averaged and nonlinear shallow water) are found in the frequency-dispersion terms—the nonlinear terms are the same. The testing method to determine the deep-water limits of the various model types will be to fix both a slope of $15°$ and a slide mass, with $\Delta h/b = 0.05$ and $L_{\rm s}/b = 1.85$, while incrementally increasing the initial water depth above the centre point of the slide, d. Figure 8 shows a summary of the comparisons of the three models. Figure $8a, d$ show the maximum free-surface depression measured above the initial centre point of the slide and the maximum rundown for various $L_{\rm s}/h_{\rm c_0}$ combinations. WNL-EXT solutions are indicated by solid lines, WNL-DA by dashed lines and NL-SW by the dotted lines. Also shown in figure $8b, e$ are the maximum depression and rundown results from WNL-DA and NL-SW relative to the results from WNL-EXT, thereby more clearly depicting the differences between the models. These figures show WNL-EXT and WNL-DA agreeing nearly exactly, while the errors in NL-SW decrease with increasing $L_{\rm s}/h_{\rm c_0}$. The NL-SW results do not converge with the WNL-EXT results until $L_{\rm s}/h_{\rm c_0} \gtrsim 15$. Figure $8c, f$ are time-series of the free-surface elevation above the initial centre point of the slide and the vertical movement of the shoreline for the case of $L_{\rm s}/h_{\rm c_0} = 3.5$, respectively. Differences between NL-SW and WNL-EXT are clear, with NL-SW under-predicting the free surface above the slide, but over-predicting the rundown due to over shoaling in the non-dispersive model. The only significant difference between the WNL-EXT and WNL-DA results come after the maximum depression in figure $8c$, where WNL-DA predicts an oscillatory train following the depression. These results indicate that to the deep-water limit that WNL-EXT was shown to be accurate, WNL-DA is accurate as well. As mentioned previously, altering the level on which z_α is evaluated in the 'extended' model does not increase the deep-water accuracy limit for slide-generated waves.

In summary, the nonlinear-dispersive terms are important for slides near the deep-water limit ($L_{\rm s}/h_{\rm c} = 3.5$) whose heights, or $\Delta h/d_0$ values, are large (greater than 0.4). For shallow-water slides ($L_{\rm s}/h_{\rm c} > 10$), the nonlinear-dispersive terms are not important near the source, even for the largest slides. The 'extended' formulation of the depth-integrated equations does not appear to offer any benefits over the depth-averaged formulation in regards to modelling the generation of waves in deeper water. The 'extended' model would be useful if one was interested in modelling the propagation of shallow-water slide-generated waves into deeper water, which is not the focus of this paper. The shallow-water-wave equations are only valid for slides in very shallow water, where $L_{\rm s}/h_{\rm c_0} \gtrsim 15$.

9. Conclusions

A model for the creation of fully nonlinear long waves by seafloor movement, and their propagation away from the source region, is presented. The general fully nonlinear model can be truncated, so as to only include weakly nonlinear effects, or model a non-dispersive wave system. Rarely will fully nonlinear effects be important above the landslide region, but the model has the advantage of allowing the slide-generated waves to become fully nonlinear in nature, without requiring a transition among governing equations.

A high-order finite-difference model is developed to numerically simulate wave generation by seafloor movement. The numerical generation of waves by both impulsive and creeping movements agrees with experimental data and other numerical models. A deep-water accuracy limit of the model, $L_s/h_c > 3.5$, is adopted. Within this limitation, the 'extended' formulation of the depth-integrated equations shows no benefit over the 'conventional' depth-averaged approach near the source region. Leading-order nonlinear effects were shown to be important for prediction of shoreline movement, and the fully nonlinear terms are important for only the thickest slides with relatively short length-scales. Although only one-horizontal-dimension problems are examined in this paper, slides in two horizontal dimensions have been analysed by the authors, but, due to paper length limitations, will be presented in a future publication. As a final remark, it is noted that prediction of landslide tsunamis in real cases is subject to the large uncertainty inherent in knowing the time-evolution of a landslide. Extensive field research of high-risk sites is paramount to reducing this uncertainty.

Appendix A. Derivation of approximate two-dimensional governing equations

In deriving the two-dimensional depth-integrated governing equations, the frequency dispersion is assumed to be weak, i.e.

$$O(\mu^2) \ll 1. \tag{A 1}$$

We can expand the dimensionless physical variables as power series of μ^2,

$$f = \sum_{n=0}^{\infty} \mu^{2n} f_n \quad (f = \zeta, p, \boldsymbol{u}), \tag{A 2}$$

$$w = \sum_{n=1}^{\infty} \mu^{2n} w_n. \tag{A 3}$$

Furthermore, we will assume the flow is irrotational. Zero horizontal vorticity yields the following conditions:

$$\frac{\partial}{\partial z} \boldsymbol{u}_0 = 0, \tag{A 4}$$

$$\frac{\partial}{\partial z} \boldsymbol{u}_1 = \nabla w_1. \tag{A 5}$$

Consequently, from (A 4), the leading-order horizontal velocity components are independent of the vertical coordinate, i.e.

$$\boldsymbol{u}_0 = \boldsymbol{u}_0(x, y, t). \tag{A 6}$$

Substituting (A 2) and (A 3) into the continuity equation (2.3) and the boundary condition (2.7), we collect the leading-order terms as

$$\nabla \cdot \boldsymbol{u}_0 + w_{1z} = 0, \quad -h < z < \varepsilon\zeta, \tag{A 7}$$

$$w_1 + \boldsymbol{u}_0 \cdot \nabla h + \frac{h_t}{\varepsilon} = 0 \quad \text{on } z = -h. \tag{A 8}$$

Integrating (A 7) with respect to z and using (A 8) to determine the integration constant, we obtain the vertical profile of the vertical velocity components,

$$w_1 = -z\nabla \cdot \boldsymbol{u}_0 - \nabla \cdot (h\boldsymbol{u}_0) - \frac{h_t}{\varepsilon}. \tag{A 9}$$

Similarly, integrating (A 5) with respect to z, with information from (A 8), we can find the corresponding vertical profiles of the horizontal velocity components,

$$\boldsymbol{u}_1 = -\tfrac{1}{2}z^2\nabla(\nabla \cdot \boldsymbol{u}_0) - z\nabla\left[\nabla \cdot (h\boldsymbol{u}_0) + \frac{h_t}{\varepsilon}\right] + \boldsymbol{C}_1(x, y, t), \tag{A 10}$$

in which $\boldsymbol{C}_1$ is a unknown function to be determined. Up to $O(\mu^2)$, the horizontal velocity components can be expressed as

$$\boldsymbol{u} = \boldsymbol{u}_0(x, y, t)$$
$$+ \mu^2\left\{-\tfrac{1}{2}z^2\nabla(\nabla \cdot \boldsymbol{u}_0) - z\nabla\left[\nabla \cdot (h\boldsymbol{u}_0) + \frac{h_t}{\varepsilon}\right] + \boldsymbol{C}_1(x, y, t)\right\} + O(\mu^4),$$
$$-h < z < \varepsilon\zeta. \tag{A 11}$$

Now, we can define the horizontal velocity vector, $\boldsymbol{u}_\alpha(x, y, z_\alpha(x, y, t), t)$, evaluated at $z = z_\alpha(x, y, t)$, as

$$\boldsymbol{u}_\alpha = \boldsymbol{u}_0 + \mu^2\left\{-\tfrac{1}{2}z_\alpha^2\nabla(\nabla \cdot \boldsymbol{u}_0) - z_\alpha\nabla\left[\nabla \cdot (h\boldsymbol{u}_0) + \frac{h_t}{\varepsilon}\right] + \boldsymbol{C}_1(x, y, t)\right\} + O(\mu^4). \tag{A 12}$$

Subtracting (A 12) from (A 11), we can express $\boldsymbol{u}$ in terms of $\boldsymbol{u}_\alpha$ as

$$\boldsymbol{u} = \boldsymbol{u}_\alpha - \mu^2\left\{\tfrac{1}{2}z^2 - z_\alpha^2\nabla(\nabla \cdot \boldsymbol{u}_\alpha) + (z - z_\alpha)\nabla\left[\nabla \cdot (h\boldsymbol{u}_\alpha) + \frac{h_t}{\varepsilon}\right]\right\} + O(\mu^4). \tag{A 13}$$

Note that $\boldsymbol{u}_\alpha = \boldsymbol{u}_0 + O(\mu^2)$ has been used in (A 13).

The exact continuity equation (2.8) can be rewritten approximately in terms of ζ and $\boldsymbol{u}_\alpha$. Substituting (A 13) into (2.8), we obtain

$$\frac{1}{\varepsilon}H_t + \nabla \cdot (H\boldsymbol{u}_\alpha) - \mu^2\nabla \cdot \left\{H\left[(\tfrac{1}{6}(\varepsilon^2\zeta^2 - \varepsilon\zeta h + h^2) - \tfrac{1}{2}z_\alpha^2)\nabla(\nabla \cdot \boldsymbol{u}_\alpha)\right.\right.$$
$$\left.\left. + (\tfrac{1}{2}(\varepsilon\zeta - h) - z_\alpha)\nabla\left(\nabla \cdot (h\boldsymbol{u}_\alpha) + \frac{h_t}{\varepsilon}\right)\right]\right\} = O(\mu^4), \tag{A 14}$$

in which $H = h + \varepsilon\zeta$.

Equation (A 14) is one of three governing equations for ζ and $\boldsymbol{u}_\alpha$. The other two equations come from the horizontal momentum equation (2.4). However, we must

find the pressure field first. This can be accomplished by approximating the vertical momentum equation (2.5) as

$$\varepsilon p_z = -1 - \mu^2 (\varepsilon w_{1t} + \varepsilon^2 \boldsymbol{u}_0 \cdot \nabla w_1 + \varepsilon^2 w_1 w_{1z}) + O(\mu^4), \quad -h < z < \varepsilon\zeta. \quad (A\,15)$$

We can integrate the above equation with respect to z to find the pressure field as

$$\begin{aligned}
p = {} & \left(\zeta - \frac{z}{\varepsilon} \right) \\
& + \mu^2 \bigg\{ \tfrac{1}{2}(z^2 - \varepsilon^2\zeta^2)\nabla \cdot \boldsymbol{u}_{0t} + (z - \varepsilon\zeta)\left[\nabla \cdot (h\boldsymbol{u})_{0t} + \frac{h_{tt}}{\varepsilon} \right] \\
& \qquad + \tfrac{1}{2}\varepsilon(z^2 - \varepsilon^2\zeta^2)\boldsymbol{u}_0 \cdot \nabla(\nabla \cdot \boldsymbol{u}_0) + \varepsilon(z - \varepsilon\zeta)\boldsymbol{u}_0 \cdot \nabla\left[\nabla \cdot (h\boldsymbol{u}_0) + \frac{h_t}{\varepsilon} \right] \\
& \qquad + \tfrac{1}{2}\varepsilon(\varepsilon^2\zeta^2 - z^2)(\nabla \cdot \boldsymbol{u}_0)^2 + \varepsilon(\varepsilon\zeta - z)\left[\nabla \cdot (h\boldsymbol{u}_0) + \frac{h_t}{\varepsilon} \right]\nabla \cdot \boldsymbol{u}_0 \bigg\} \\
& + O(\mu^4)
\end{aligned}$$

$$(A\,16)$$

for $-h < z < \varepsilon\zeta$. We remark here that (A 11) has been used in deriving (A 16). To obtain the governing equations for $\boldsymbol{u}_\alpha$, we first substitute (A 13) and (A 16) into (2.4) and obtain the following equation, up to $O(\mu^2)$,

$$\begin{aligned}
\boldsymbol{u}_{\alpha t} &+ \varepsilon\boldsymbol{u}_\alpha \cdot \nabla\boldsymbol{u}_\alpha + \nabla\zeta \\
& + \mu^2 \bigg\{ \tfrac{1}{2}z_\alpha^2 \nabla(\nabla \cdot \boldsymbol{u}_{\alpha t}) + z_\alpha \nabla\left[\nabla \cdot (h\boldsymbol{u}_\alpha)_t + \frac{h_{tt}}{\varepsilon} \right] \bigg\} \\
& + \mu^2 z_{\alpha t} \bigg\{ z_\alpha \nabla(\nabla \cdot \boldsymbol{u}_\alpha) + \nabla\left[\nabla \cdot (h\boldsymbol{u}_\alpha) + \frac{h_t}{\varepsilon} \right] \bigg\} \\
& + \varepsilon\mu^2 \bigg\{ \left[\nabla \cdot (h\boldsymbol{u}_\alpha) + \frac{h_t}{\varepsilon} \right]\nabla\left[\nabla \cdot (h\boldsymbol{u}_\alpha) + \frac{h_t}{\varepsilon} \right] \\
& \qquad - \nabla\left[\zeta\left(\nabla \cdot (h\boldsymbol{u}_\alpha)_t + \frac{h_{tt}}{\varepsilon} \right) \right] + (\boldsymbol{u}_\alpha \cdot \nabla z_\alpha)\nabla\left[\nabla \cdot (h\boldsymbol{u}_\alpha) + \frac{h_t}{\varepsilon} \right] \\
& \qquad + z_\alpha \nabla\left[\boldsymbol{u}_\alpha \cdot \nabla\left(\nabla \cdot (h\boldsymbol{u}_\alpha) + \frac{h_t}{\varepsilon} \right) \right] + z_\alpha(\boldsymbol{u}_\alpha \cdot \nabla z_\alpha)\nabla(\nabla \cdot \boldsymbol{u}_\alpha) \\
& \qquad\qquad + \tfrac{1}{2}z_\alpha^2 \nabla[\boldsymbol{u}_\alpha \cdot \nabla(\nabla \cdot \boldsymbol{u}_\alpha)] \bigg\} \\
& + \varepsilon^2\mu^2 \nabla \bigg\{ -\tfrac{1}{2}\zeta^2 \nabla \cdot \boldsymbol{u}_{\alpha t} - \zeta\boldsymbol{u}_\alpha \cdot \nabla\left[\nabla \cdot (h\boldsymbol{u}_\alpha) + \frac{h_t}{\varepsilon} \right] \\
& \qquad\qquad + \zeta\left[\nabla \cdot (h\boldsymbol{u}_\alpha) + \frac{h_t}{\varepsilon} \right]\nabla \cdot \boldsymbol{u}_\alpha \bigg\} \\
& + \varepsilon^3\mu^2 \nabla \bigg\{ \tfrac{1}{2}\zeta^2[(\nabla \cdot \boldsymbol{u}_\alpha)^2 - \boldsymbol{u}_\alpha \cdot \nabla(\nabla \cdot \boldsymbol{u}_\alpha)] \bigg\} = O(\mu^4).
\end{aligned}$$

$$(A\,17)$$

Equations (A 14) and (A 17) are the coupled governing equations, written in terms of $\boldsymbol{u}_\alpha$ and ζ, for fully nonlinear weakly dispersive waves generated by a submarine landslide.

Appendix B. Numerical scheme

To simplify the predictor-corrector equations, the velocity time derivatives in the momentum equations are grouped into the dimensional form,

$$U = u + \tfrac{1}{2}(z_\alpha^2 - \zeta^2)u_{xx} + (z_\alpha - \zeta)(hu)_{xx} - \zeta_x[\zeta u_x + (hu)_x], \tag{B 1}$$

$$V = v + \tfrac{1}{2}(z_\alpha^2 - \zeta^2)v_{yy} + (z_\alpha - \zeta)(hv)_{yy} - \zeta_y[\zeta v_y + (hv)_y], \tag{B 2}$$

where subscripts denote partial derivatives. Note that this grouping is different from that given in Wei *et al.* (1995). The grouping given above in (B 1) and (B 2) incorporates nonlinear terms, which is not done in Wei *et al.* These nonlinear time derivatives arise from the nonlinear-dispersion terms $\nabla[\zeta(\nabla \cdot (h\boldsymbol{u}_\alpha)_t + h_{tt}/\varepsilon)]$ and $\nabla(\tfrac{1}{2}\zeta^2\nabla \cdot \boldsymbol{u}_{\alpha t})$, which can be reformulated using the relation

$$\nabla\left[\zeta\left(\nabla \cdot (h\boldsymbol{u}_\alpha)_t + \frac{h_{tt}}{\varepsilon}\right)\right]$$
$$= \nabla\left[\zeta\left(\nabla \cdot (h\boldsymbol{u}_\alpha) + \frac{h_t}{\varepsilon}\right)\right]_t - \nabla\left[\zeta_t\left(\nabla \cdot (h\boldsymbol{u}_\alpha) + \frac{h_t}{\varepsilon}\right)\right]\nabla(\tfrac{1}{2}\zeta^2\nabla \cdot \boldsymbol{u}_{\alpha t})$$
$$= \nabla(\tfrac{1}{2}\zeta^2\nabla \cdot \boldsymbol{u}_\alpha)_t - \nabla(\zeta\zeta_t\nabla \cdot \boldsymbol{u}_\alpha).$$

The authors have found that this form is more stable and requires less iterations to converge for highly nonlinear problems, as compared to the Wei *et al.* formulation. The predictor equations are

$$\eta_{i,j}^{n+1} = \eta_{i,j}^n + \tfrac{1}{12}\Delta t(23E_{i,j}^n - 16E_{i,j}^{n-1} + 5E_{i,j}^{n-2}), \tag{B 3}$$

$$U_{i,j}^{n+1} = U_{i,j}^n + \tfrac{1}{12}\Delta t(23F_{i,j}^n - 16F_{i,j}^{n-1} + 5F_{i,j}^{n-2}) + 2(F_1)_{i,j}^n - 3(F_1)_{i,j}^{n-1} + (F_1)_{i,j}^{n-2}, \tag{B 4}$$

$$V_{i,j}^{n+1} = V_{i,j}^n + \tfrac{1}{12}\Delta t(23G_{i,j}^n - 16G_{i,j}^{n-1} + 5G_{i,j}^{n-2}) + 2(G_1)_{i,j}^n - 3(G_1)_{i,j}^{n-1} + (G_1)_{i,j}^{n-2}, \tag{B 5}$$

where

$$\begin{aligned}
E = {}& -h_t - [(\zeta + h)u]_x - [(\zeta + h)v]_y \\
& + \{(h + \zeta)[(\tfrac{1}{6}(\zeta^2 - \zeta h + h^2) - \tfrac{1}{2}z_\alpha^2)S_x + (\tfrac{1}{2}(\zeta - h) - z_\alpha)T_x]\}_x \\
& + \{(h + \zeta)[(\tfrac{1}{6}(\zeta^2 - \zeta h + h^2) - \tfrac{1}{2}z_\alpha^2)S_y + (\tfrac{1}{2}(\zeta - h) - z_\alpha)T_y]\}_y,
\end{aligned} \tag{B 6}$$

$$\begin{aligned}
F = {}& -\tfrac{1}{2}[(u^2)_x + (v^2)_x] - g\zeta_x - z_\alpha h_{xtt} - z_{\alpha t}h_{xt} + (\zeta h_{tt})_x - [E(\zeta S + T)]_x \\
& - [\tfrac{1}{2}(z_\alpha^2 - \zeta^2)(uS_x + vS_y)]_x - [(z_\alpha - \zeta)(uT_x + vT_y)]_x - \tfrac{1}{2}[(T + \zeta S)^2]_x,
\end{aligned} \tag{B 7}$$

$$F_1 = \tfrac{1}{2}(\zeta^2 - z_\alpha^2)v_{xy} - (z_\alpha - \zeta)(hv)_{xy} + \zeta_x[\zeta v_y + (hv)_y], \tag{B 8}$$

$$\begin{aligned}
G = {}& -\tfrac{1}{2}[(u^2)_y + (v^2)_y] - g\zeta_y - z_\alpha h_{ytt} - z_{\alpha t}h_{yt} + (\zeta h_{tt})_y - [E(\zeta S + T)]_y \\
& - [\tfrac{1}{2}(z_\alpha^2 - \zeta^2)(uS_x + vS_y)]_y - [(z_\alpha - \zeta)(uT_x + vT_y)]_y - \tfrac{1}{2}[(T + \zeta S)^2]_y,
\end{aligned} \tag{B 9}$$

$$G_1 = \tfrac{1}{2}(\zeta^2 - z_\alpha^2)u_{xy} - (z_\alpha - \zeta)(hu)_{xy} + \zeta_y[\zeta u_x + (hu)_x] \tag{B 10}$$

and

$$S = u_x + v_y, \qquad T = (hu)_x + (hv)_y + h_t. \tag{B 11}$$

All terms are evaluated at the local grid point (i, j), and n represents the current time-step, when values of ζ, u and v are known. The above expressions (B 6)–(B 11) are for the fully nonlinear problem; if a weakly nonlinear or non-dispersive system is to be examined, the equations should be truncated accordingly. The fourth-order implicit corrector expressions for the free-surface elevation and horizontal velocities are

$$\eta_{i,j}^{n+1} = \eta_{i,j}^n + \tfrac{1}{24}\Delta t(9E_{i,j}^{n+1} + 19E_{i,j}^n - 5E_{i,j}^{n-1} + E_{i,j}^{n-2}), \tag{B 12}$$

$$U_{i,j}^{n+1} = U_{i,j}^n + \tfrac{1}{24}\Delta t(9F_{i,j}^{n+1} + 19F_{i,j}^n - 5F_{i,j}^{n-1} + F_{i,j}^{n-2}) + (F_1)_{i,j}^{n+1} - (F_1)_{i,j}^n, \tag{B 13}$$

$$V_{i,j}^{n+1} = V_{i,j}^n + \tfrac{1}{24}\Delta t(9G_{i,j}^{n+1} + 19G_{i,j}^n - 5G_{i,j}^{n-1} + G_{i,j}^{n-2}) + (G_1)_{i,j}^{n+1} - (G_1)_{i,j}^n. \tag{B 14}$$

The system is solved by first evaluating the predictor equations, then u and v are solved via (B 1) and (B 2), respectively. Both (B 1) and (B 2) yield a diagonal matrix after finite differencing. The matrices are diagonal, with a bandwidth of five (due to five-point finite differencing), and an efficient LU decomposition can be used. At this point in the numerical system, we have predictors for ζ, u and v. Next, the corrector expressions are evaluated, and again u and v are determined from (B 1) and (B 2). The relative errors in each of the physical variables is found, in order to determine if the implicit correctors need to be reiterated. This relative error is given as

$$\frac{w^{n+1} - w_*^{n+1}}{w^{n+1}}, \tag{B 15}$$

where w represents ζ, u and v, and w_* is the previous iterations value. The correctors are recalculated until all errors are less than 10^{-4}. Note that, inevitably, there will be locations in the numerical domain where values of the physical variables are close to zero, and applying the above error calculation to these points may lead to unnecessary iterations in the corrector loop. Thus it is required that

$$\left| \frac{\zeta}{a} \right|, \left| \frac{u, v}{\epsilon\sqrt{gh}} \right| > 10^{-4}$$

for the corresponding error calculation to proceed, where a is determined from equation (3.4) for a creeping slide. For the model equations, linear stability analysis gives that $\Delta t < \Delta x/2c$, where c is the wave celerity in the deepest water. Note that when modelling highly nonlinear waves, a smaller Δt is usually required for stability. In this analysis, $\Delta t = \Delta x/4c$ produced stable and convergent results for all trails.

For the numerical exterior boundaries, two types of conditions are applied: reflective and radiation. The reflective, or no-flux, boundary condition for the Boussinesq equations has been examined by previous researchers (Wei & Kirby 1995), and their methodology is followed here. For the radiation, or open, boundary condition, a sponge layer is used. The sponge layer is applied in the manner recommended by Kirby *et al.* (1998). Run-up and rundown are modelled with the 'extrapolation' moving-boundary algorithm described in Lynett *et al.* (2002).

Nomenclature

a	wave amplitude
b	length along the slope between x_l and x_r for the tanh slide
c	wave celerity
d	depth of water above the centre point of the slide, function of time
d_0	initial depth of water above the centre point of the slide, i.e. at $t = 0$
g	gravity
h_0	characteristic water depth or baseline water depth, function of space
h	water depth profile, function of space and time
$\bar{h}$	the changing part of the water depth profile $((h - h_0)/\delta)$
h_c	baseline water depth at the centre point of the slide $(\Delta h + d)$
h_{c_0}	initial baseline water depth at the centre point of the slide $(\Delta h + d_0)$
H	total water depth $(h + \varepsilon\zeta)$
l_0	characteristic horizontal length-scale of the submarine slide
L_s	characteristic horizontal side length of the submarine slide
p	depth-dependent pressure
S	shape factor for tanh slide
t	time
t_c	time-scale of seafloor motion
t_w	typical period of wave generated by a specified seafloor motion
u, v, w	depth-dependent components of velocity in x, y, z
u_α, v_α	magnitude of horizontal velocity components u, v evaluated on z_α
$\bar{u}, \bar{v}$	depth-averaged horizontal velocity components
$\boldsymbol{u}$	horizontal velocity vector, (u, v)
x_c, y_c	horizontal coordinates of the midpoint of the seafloor movement
x_l, x_r	locations of the left and right inflection points for the tanh slide profile
z_α	arbitrary level on which the 'extended' equations are derived
δ	scaled characteristic change in water depth due to seafloor motion $(\Delta h/h_0)$
Δh	characteristic, or maximum, change in water depth due to seafloor motion
Δt	time-step in numerical model
$\Delta x, \Delta y$	space steps in numerical model
ε	nonlinearity parameter (a/h_0)
∇	horizontal gradient vector
ρ	density of water
θ	slope angle
μ	frequency-dispersion parameter (h_0/l_0)
ζ	free-surface displacement

References

Chen, Y. & Liu, P. L.-F. 1995 Modified Boussinesq equations and associated parabolic model for water wave propagation. *J. Fluid Mech.* **228**, 351–381.

Cox, D. C. & Morgan, J. 1977 Local tsunamis and possible local tsunamis in Hawaii. Report no. HIG 77-14, Hawaii Institute of Geophysics, University of Hawaii.

Forbes, L. K. & Schwartz, L. W. 1982 Free-surface flow over a semicircular obstruction. *J. Fluid Mech.* **114**, 299–314.

Geist, E. L. 1998 Local tsunami and earthquake source parameters. *Adv. Geophys.* **39**, 117–209.

Gobbi, M., Kirby, J. T. & Wei, G. 2000 A fully nonlinear Boussinesq model for surface waves. Part 2. Extension to $O(kh^4)$. *J. Fluid Mech.* **405**, 181–210.

Grilli, S. T. 1993 Modeling of nonlinear wave motion in shallow water. In *Computational methods for free and moving boundary problems in heat and fluid flows* (ed. I. C. Wrobel & C. A. Brebbia), ch. 3, pp. 37–65. Elsevier.

Grilli, S. T. & Watts, P. 1999 Modeling of waves generated by a moving submerged body. Applications to underwater landslides. *Engng Analysis Bound. Elem.* **23**, 645–656.

Grilli, S. T., Skourup, J. & Svendsen, I. A. 1989 An efficient boundary element method for nonlinear waves. *Engng Analysis Bound. Elem.* **6**, 97–107.

Grilli, S. T., Subramanya, R., Svendsen, I. A. & Veeramony, J. 1995 Shoaling of solitary waves on plane beaches. *J. Wtrwy Port Coastal Ocean Engng* **120**, 74–92.

Hammack, H. L. 1973 A note on tsunamis: their generation and propagation in an ocean of uniform depth. *J. Fluid Mech.* **60**, 769–799.

Harbitz, C. B., Pedersen, G. & Gjevik, B. 1993 Numerical simulation of large water waves due to landslides. *J. Hydraul. Engng* **119**, 1325–1342.

Jiang, L. & LeBlond, P. H. 1992 The coupling of a submarine slide and the surface waves which it generates. *J. Geophys. Res.* **97**, 12 731–12 744.

Keating, B. H. & McGuire, W. J. 2002 Island edifice failures and associated hazards. In *Pure and applied geophysics, special issue: landslide and tsunamis.* (In the press.)

Kirby, J. T., Wei, G., Chen, Q., Kennedy, A. B. & Dalrymple, R. A. 1998 *FUNWAVE 1.0: fully nonlinear Boussinesq wave model documentation and user's manual*. Newark, DE: University of Delaware.

Lee, S.-J., Yates, G. T. & Wu, T. Y. 1989 Experiments and analyses of upstream-advancing solitary waves generated by moving disturbances. *J. Fluid Mech.* **199**, 569–593.

Liu, P. L.-F. 1994 Model equations for wave propagations from deep to shallow water. In *Advances in coastal and ocean engineering* (ed. P. L.-F. Liu), vol. 1, pp. 125–158. World Scientific.

Liu, P. L.-F. & Earickson, J. 1983 A numerical model for tsunami generation and propagation. In *Tsunamis: their science and engineering* (ed. J. Iida & T. Iwasaki), pp. 227–240. Harpenden: Terra Science.

Liu, P. L.-F., Hsu, H.-W. & Lean, M. H. 1992 Applications of boundary integral equation methods for two-dimensional non-linear water wave problems. *Int. J. Numer. Meth. Fluids* **15**, 1119–1141.

Lynett, P., Wu, T.-W. & Liu, P. L.-F. 2002 Modeling wave runup with depth-integrated equations. *Coastal Engng* **46**, 89–107.

Madsen, P. A. & Schäffer, H. A. 1998 Higher-order Boussinesq-type equations for surface gravity waves: derivation and analysis. *Phil. Trans. R. Soc. Lond.* A **356**, 2123–3184.

Madsen, P. A. & Sorensen, O. R. 1992 A new form of the Boussinesq equations with improved linear dispersion characteristics. Part II. A slowly varying bathymetry. *Coastal Engng* **18**, 183–204.

Moore, G. & Moore, J. G. 1984 Deposit from giant wave on the island of Lanai. *Science* **222**, 1312–1315.

Nwogu, O. 1993 Alternative form of Boussinesq equations for nearshore wave propagation. *J. Wtrwy Port Coastal Ocean Engng* **119**, 618–638.

Peregrine, D. H. 1967 Long waves on a beach. *J. Fluid Mech.* **27**, 815–827

Press, W. H., Flannery, B. P. & Teukolsky, S. A. 1989 *Numerical recipes: the art of scientific computing*, pp. 569–572. Cambridge University Press.

Raney, D. C. & Butler, H. L. 1976 Landslide generated water wave model. *J. Hydraul. Div.* **102**, 1269–1282.

Tappin, D. R. (and 18 others) 1999 Sediment slump likely caused 1998 Papua New Guinea tsunami. *Eos* **80**, 329.

Tappin, D. R., Watts, P., McMurtry, G. M., Lafoy, Y. & Matsumoto, T. 2001 The Sissano, Papau New Guinea tsunami of July 1998—offshore evidence on the source mechanism. *Mar. Geol.* **175**, 1–23.

von Huene, R., Bourgois, J., Miller, J. & Pautot, G. 1989 A large tsunamigetic landslide and debris flow along the Peru trench. *J. Geophys. Res.* **94**, 1703–1714.

Watts, P. 1997 Water waves generated by underwater landslides. PhD thesis, California Institute of Technology.

Wei, G. & Kirby, J. T. 1995 A time-dependent numerical code for extended Boussinesq equations. *J. Wtrwy Port Coastal Ocean Engng* **120**, 251–261.

Wei, G., Kirby, J. T., Grilli, S. T. & Subramanya, R. 1995 A fully nonlinear Boussinesq model for surface waves. Part 1. Highly nonlinear unsteady waves. *J. Fluid Mech.* **294**, 71–92.

Yeh, H., Liu, P. L.-F. & Synolakis, C. (eds) 1996 Long-wave runup models. In *Proc. 2nd Int. Workshop on Long-wave Runup Models*. World Scientific.